J. Fluid Mech. (2023), *vol.* 971, A41, doi:10.1017/jfm.2023.709

Finite Froude and Rossby numbers counter-rotating vortex pairs

Jean N. Reinaud†

School of Mathematics and Statistics, University of St Andrews, St Andrews KY16 9SS, UK

(Received 20 March 2023; revised 24 July 2023; accepted 22 August 2023)

We investigate the nonlinear evolution of pairs of three-dimensional, equal-sized and opposite-signed vortices at finite Froude and Rossby numbers. The two vortices may be offset in the vertical direction. The initial conditions stem from relative equilibria obtained numerically in the quasi-geostrophic regime, for vanishing Froude and Rossby numbers. We first address the linear stability of the quasi-geostrophic opposite-signed pairs of vortices, and show that for all vertical offsets, the vortices are sensitive to an instability when close enough together. In the nonlinear regime, the instability may lead to the partial destruction of the vortices. We then address the nonlinear interaction of the vortices for various values of the Rossby number. We show that as the Rossby number increases, destructive interactions, where the vortices break into pieces, may occur for a larger separation between the vortices, compared to the quasi-geostrophic case. We also show that for well-separated vortices, the interaction is non-destructive, and ageostrophic effects lead to the deviation of the trajectory of the pair of vortices, as the anticyclonic vortex dominates the interaction. Finally, we show that the flow remains remarkably close to a balanced state, emitting only waves containing negligible energy, even when the interaction leads to the destruction of the vortices.

Key words: vortex instability, vortex interactions

1. Introduction

Vortices are key dynamical features of the atmosphere and the oceans. Collectively, they contribute to a significant part of the mass transport in the oceans (Zhang, Wang & Qiu 2014). When two opposite-signed vortices are close together, they interact strongly and

† Email address for correspondence: jnr1@st-andrews.ac.uk

form a pair that self-propagates in the flow (de Ruijter *et al.* 2004; L'Hegaret *et al.* 2014). Typically, the distance separating the vortices remains nearly constant in time, at least until the pair interacts strongly with another feature. Such pairs of vortices are sometimes referred to as dipoles, and they can transport momentum, mass and tracers efficiently over long distances in the fluid. Recent analyses of altimetry data have shown that dipoles are widespread in the global ocean (Ni *et al.* 2020).

Dipoles also include mushroom-like currents that abound in the oceans (Fedorov & Ginsburg 1989). Other families of dipoles include modons on the β-plane (Stern 1975; Larichev & Reznik 1976) and on the f-plane (Kizner *et al.* 2008), to name but a few examples. Other examples are the hetons introduced by Hogg & Stommel (1985) where the two opposite-signed vortices occupy distinct depths. These vortices will not be considered in the present paper.

Pallàs-Sanz & Viúdez (2007) investigated numerically the ageostrophic motion of a specific family of pairs of opposite-signed vortices where the two vortices are ellipsoids of uniform potential vorticity. The authors showed that ageostrophic effects affect the trajectory of the dipole as the anticyclonic vortex tends to be larger and more intense. In their study, the vortices in the dipole remained well-separated and the vortices retained their volume.

In the present work, we determine numerically pairs of opposite-signed, uniform potential vorticity (PV) vortices in mutual equilibrium under the quasi-geostrophic (QG) approximation, for vanishing Rossby (Ro) and Froude (Fr) numbers, on the f-plane. These equilibria are then used to initialise numerical simulations at finite Ro and Fr. This choice helps the vortices to remain close to an equilibrium for small Ro, and therefore limits vortex deformations otherwise associated with another arbitrary choice of initial conditions. It also limits the spontaneous generation of inertia-gravity waves and allows the flow to remain close to a balanced state. We show that both under the QG approximation and at finite Ro and Fr numbers, the pair of vortices undergoes a destructive interaction when the distance separating them is less than a threshold that we determine. For non-destructive interactions, where the vortices retain their material, we quantify the dynamical asymmetry between the cyclonic and the anticyclonic vortices by measuring a QG-equivalent PV ratio. This is the PV ratio of a pair of QG vortices having the same trajectory.

The paper is organised as follows. Pairs of counter-rotating vortices in mutual equilibria under the QG approximation are presented in § 2. Section 3 is devoted to the nonlinear evolution of the vortex pairs at finite Ro and Fr numbers. Conclusions are given in § 4.

2. Quasi-geostrophic equilibria

We first consider pairs of counter-rotating vortices under the QG approximation. Under this approximation, the full flow fields can be recovered from a single scalar field q, the QG PV anomaly, hereinafter referred to as PV for simplicity. In the form used in this study, the QG equations are obtained by a Rossby number expansion of Euler's equations for a rotating fluid under the Boussinesq approximation with $Fr^2 \ll Ro \ll 1$. Here, $Ro = U/(fL)$ is the Rossby number, while $Fr = U/(NH)$ is the Froude number; U is a characteristic scale of horizontal velocity, f is the Coriolis frequency, N is the buoyancy (or Brunt–Väisälä) frequency, and L and H are horizontal and vertical length scales, respectively. A complete derivation may be found in Vallis (2006). For simplicity, we assume that both f and N are constant. The PV q may be defined as the modified three-dimensional Laplacian of a streamfunction φ:

$$q = \frac{\partial^2 \varphi}{\partial x^2} + \frac{\partial^2 \varphi}{\partial y^2} + \frac{f^2}{N^2}\frac{\partial^2 \varphi}{\partial z^2} = \mathcal{L}_{QG}(\varphi). \tag{2.1}$$

The PV q is conserved materially in the absence of diabatic or dissipative effects:

$$\frac{\partial q}{\partial t} + u\frac{\partial q}{\partial x} + v\frac{\partial q}{\partial y} = 0, \tag{2.2}$$

where the advecting velocity field $\boldsymbol{u} = (u, v, 0)$ is the non-divergent geostrophic velocity deriving from the streamfunction φ as

$$u = -\frac{\partial \varphi}{\partial y}, \quad v = \frac{\partial \varphi}{\partial x}. \tag{2.3\textit{a,b}}$$

Finally the buoyancy anomaly is recovered from φ via

$$b = f\frac{\partial \varphi}{\partial z}. \tag{2.4}$$

It is important to notice that there is no dynamical asymmetry between a cyclonic vortex ($q > 0$) and an anticyclonic vortex ($q < 0$) in QG.

We consider two vortices of uniform PV $\pm q_r$, with $q_r > 0$ without loss of generality. We denote as vortex 1 the vortex with PV $q_1 = -q_r$, and as vortex 2 the vortex with $q_2 = q_r$. The vortices have the same volume $\mathcal{V}_1 = \mathcal{V}_2 = \mathcal{V}$, hence the same strength in absolute value $|\kappa_1| = |\kappa_2|$, where $\kappa_i \equiv (4\pi)^{-1} q_i \mathcal{V}_i$. We set $q_r = 2\pi$, implicitly defining a time scale for the problem. For example, the rotation period of a single sphere, in the $(x, y, zN/f)$ coordinate system, of uniform PV q_r is $T = 6\pi/q_r = 3$ here. Each vortex is centred at $\boldsymbol{x}_i$. We denote the vertical offset between the vortices as $\Delta z = z_2 - z_1 \geq 0$ without loss of generality. Recall that the absence of vertical advection under the QG approximation implies that $z_i =$ const. The fluid domain is unbounded in all three directions of space.

We determine numerically the shape of the vortices in mutual equilibrium, translating steadily at a constant velocity V in the unbounded fluid domain. It should be noted that Reinaud & Dritschel (2009) have already determined equilibria for pairs of unequal-sized counter-rotating vortices, albeit at lower resolution. In this case, the pairs rotate rather than translate. The present choice of translating vortices is to emphasise the dynamical asymmetry due to ageostrophic effects discussed in § 3. In this present study and without loss of generality, the vortex centres are horizontally aligned along the y-direction and separated in the x-direction. Thus the vortices translate in the y-direction. The boundary of each vortex is discretised in the vertical direction by n_c horizontal layers. In each layer, the vortex boundary is defined by a contour. For the pair of vortices, there are $2n_c$ contours, denoted $\mathcal{C}_k$, $1 \leq k \leq 2n_c$. We use an iterative procedure that makes the contours $\mathcal{C}_k$ converge to streamlines in the reference frame translating with the vortices:

$$\tilde{\varphi}(\boldsymbol{x}) = \varphi(\boldsymbol{x}) - Vx = C_k, \quad \forall \boldsymbol{x} = (x, y, z) \in \mathcal{C}_k, \tag{2.5}$$

where C_k is a constant depending on the contour $\mathcal{C}_k$, and $\tilde{\varphi}$ is the streamfunction expressed in the reference frame translating at velocity V. Details of the method may be found in previous works, e.g. Reinaud & Dritschel (2002) and Reinaud (2019). For a given vertical offset Δz, we start with vortices that are well separated in the horizontal direction by a distance Δx_{init}. The initial guess for the vortex shape is a sphere in the $(x, y, zN/f)$ coordinate system. This is motivated by the fact that a pair of spherical vortices

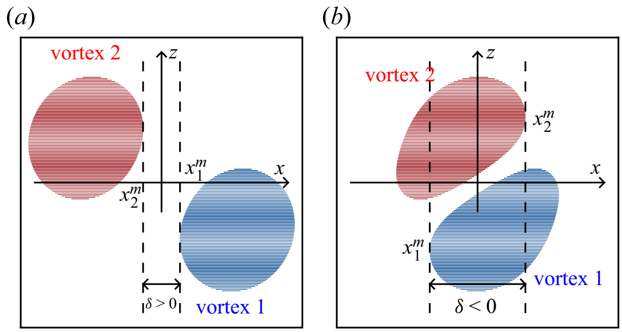

Figure 1. Definition of the innermost gap $\delta = x_1^m - x_2^m$, the signed distance between the innermost edges of vortex 1 and vortex 2. The cyclonic vortex ($q > 0$) is henceforth shown in red, while the anticyclonic vortex ($q < 0$) is shown in blue.

infinitely separated in the horizontal direction would indeed be in equilibrium. Indeed, any axisymmetric vortex standing alone is a steady state. We can also note that all vortices in this study have a mean unit height-to-width aspect ratio in the $(x, y, zN/f)$ coordinate system.

We take $x_1 > 0$ for the first equilibrium. When the equilibrium is reached, the vortices are pushed slightly together by a small distance δ', and the numerical procedure is resumed for the new horizontal separation. The procedure is repeated until the method fails to converge, corresponding to the end of the numerical branch of solutions. Hence, for a given Δz, we determine a family of equilibria spanned by the horizontal distance between the vortices. For this horizontal distance, it is convenient to use the innermost gap $\delta = x_1^m - x_2^m$, the distance between the two innermost edges x_i^m of the vortices as shown in figure 1. Note that δ can reach negative values when the vortices are vertically offset.

We also address the linear stability of the equilibria. Details of the method may also be found in previous works, e.g. Reinaud & Dritschel (2002) and Reinaud (2019). The method analyses the deformation modes of the vortex bounding contours by considering infinitesimal disturbances on the horizontal position vector $\boldsymbol{\rho}_k(\tilde{\theta}, t)$ of the nodes along the contour $\mathcal{C}_k$:

$$\boldsymbol{\rho}_k(\tilde{\theta}, t) = \boldsymbol{\rho}_{e,k}(\tilde{\theta}) + \gamma_k(\tilde{\theta}, t)\, \frac{(-\mathrm{d}y_{e,k}/\mathrm{d}\tilde{\theta}, \mathrm{d}x_{e,k}/\mathrm{d}\tilde{\theta})}{(\mathrm{d}x_{e,k}/\mathrm{d}\tilde{\theta})^2 + (\mathrm{d}y_{e,k}/\mathrm{d}\tilde{\theta})^2}, \tag{2.6}$$

where $\boldsymbol{\rho}_{e,k} = (x_{e,k}, y_{e,k})$ is the position vector at equilibrium, and $\tilde{\theta}$ is the 'travel-time coordinate', an angle proportional to the time taken by a fluid particle to travel along the contour $\mathcal{C}_k$. The disturbance γ_k is taken in the form

$$\gamma_k(\tilde{\theta}, t) = \mathrm{e}^{\sigma t} \sum_{m=1}^{M} \hat{\gamma}_{m,k}\, \mathrm{e}^{\mathrm{i}m\tilde{\theta}}, \tag{2.7}$$

where m is the mode's azimuthal wavenumber, and M is the maximum wavenumber considered in the study. The evolution equation for γ_k is given by

$$\frac{\partial \gamma_k}{\partial t} + \omega_k \frac{\partial \gamma_k}{\partial \tilde{\theta}} = -\sum_{l=1}^{2n_c} \Delta q_l \frac{\partial}{\partial \tilde{\theta}} \oint_{\mathcal{C}_l} \gamma_l\, G_{k,l}\left(\left|\boldsymbol{\rho}_{e,k}(\tilde{\theta}) - \boldsymbol{\rho}_{e,l}(\tilde{\theta}')\right|\right) \mathrm{d}\tilde{\theta}', \tag{2.8}$$

where ω_k is the constant rotation rate of a fluid particle along the contour $\mathcal{C}_k$, $\Delta q_l = \pm q_r$ is the PV jump across the contour $\mathcal{C}_l$, and $G_{k,l}$ is the Green's function giving the velocity

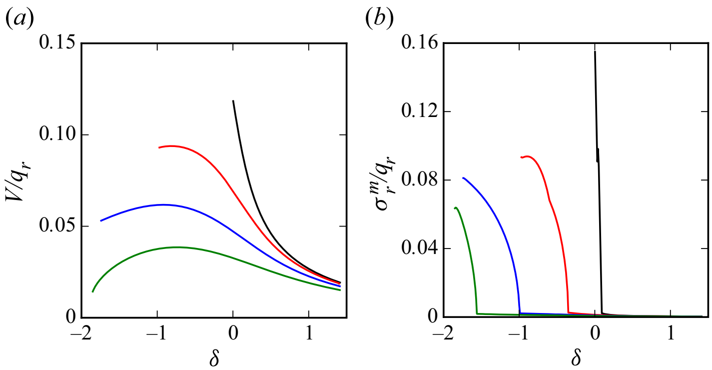

Figure 2. (*a*) Translation velocity V of the equilibria, and (*b*) maximum growth rate σ_r^m, both scaled by the reference PV q_r, versus the innermost gap δ for the relative vertical offset $\Delta z = 0$ (black lines) and $\Delta z/H = 21/83$ (red lines), $41/83$ (blue lines), $62/83$ (green lines).

induced in the layer containing the contour $\mathcal{C}_k$ in the layer containing the contour $\mathcal{C}_l$ in the unbounded fluid domain.

In this study, we set $M = 10$, which is enough to capture the onset of instability from previous experience (Reinaud & Dritschel 2009). Substituting (2.7) into (2.8) results in a $4 \times n_c \times M$ real eigenvalue problem where $\sigma = \sigma_r + \mathrm{i}\sigma_i$ is a complex eigenvalue. The real part σ_r of σ is the mode's growth rate, and the imaginary part σ_i of σ is its frequency.

In this study, we set $n_c = 83$ for a fine vertical discretisation of the vortices. Symmetry with respect to the plane $y = 0$ is imposed. Half of each contour $\mathcal{C}_k$ is discretised using $n_p = 330$ nodes to ensure high accuracy. The total volume of PV, in the $(x, y, zN/f)$ coordinate system, is set to $4\pi/3$. The mean radius of each vortex in this coordinate system is therefore $r_v = (1/2)^{1/3}$. We denote $H = 2r_v = 2^{2/3}$ as the total height of each vortex. The vertical offset Δz between the vortices is taken, for convenience, as a fraction, in number of layers, of the total height H. In this study, we consider $\Delta z/H = 0, 21/83, 41/83, 62/83$, so offsets of 0, ∼25 %, ∼50 % and ∼75 % of the vortex height. For each value of Δz, we start the calculation with $\Delta x_{init} = 3$, and we used $\delta' = 0.01$ between equilibria.

Figure 2(*a*) shows the translation velocity V of the vortex pair at equilibrium as a function of the innermost gap δ. For $\Delta z = 0$, the velocity increases monotonically as the gap δ decreases and the vortices interact more strongly. For $\Delta z \neq 0$, the velocity is no longer a monotonic function for the gap for $\delta < 0$. This can be explained easily by the fact that for a pair of opposite-signed QG point vortices, the translation velocity is $\propto \delta x/(\delta x^2 + \delta z^2)^{3/2}$ – where δx and δz are the horizontal and vertical separations between the point vortices, respectively – and has an extremum for $\delta x = \delta z/\sqrt{2}$. In figure 2(*a*), V is also affected by the shape of the finite-core vortices in equilibrium and the vertical overlap of the vortices for $\delta < 0$. The translation velocity V also decreases with the vertical offset Δz as the vortices are further apart, weakening their interaction. Figure 2(*b*) shows the maximum growth rate σ_r^m versus the gap δ. For all Δz, the pair of vortices is in a neutrally stable equilibrium with $\sigma_r^m \simeq 0$ for large δ. The residual non-zero values for large δ are due to the finite numerical accuracy of both the numerical determination of the equilibria and the linear stability analysis itself. As δ is further decreased, a first mode of instability, corresponding to $\sigma_r^m > 0$, appears at a critical value of the gap δ_c that depends on the vertical offset Δz. The values of δ_c are reported in table 1. As Δz increases, the interaction between the vortices weakens for a given δ, and δ_c decreases. It is, however, interesting

$\Delta z/H$	0	21/83	41/83	62/82
δ_c	0.08	−0.36	−1.00	−1.57
d_{3D}	0.978	1.044	1.056	1.22

Table 1. Critical gap δ_c for the four values of relative vertical offset $\Delta z/H$ considered, and corresponding vortex centroid separation d_{3D}.

to notice that the distance d_{3D} between the two vortex centroids at the margin of stability, also given in table 1, increases with Δz. This shows that vortices are particularly sensitive to vertical shear, which is enhanced by increasing moderately the vertical offset Δz. A similar trend is observed at the margin of stability of pairs of co-rotating QG vortices (Reinaud & Dritschel 2002, 2005) and the importance of vertical shear is also shown in QG turbulence (Reinaud, Dritschel & Koudella 2003). Since the vortices exert on each other both horizontal and vertical shear, the instabilities have both barotropic and baroclinic components. We conjecture that for Δz small, the instability is dominated by barotropic effects, while baroclinic effects increase continuously as Δz is increased. For $\Delta z/H > 1$ (not considered in the present paper), the pair of opposite-signed vortices is referred to as a heton, and the instability is mostly baroclinic in nature.

Figure 3 shows the shape of the vortices at equilibrium for the first unstable state, i.e. for $\delta = \delta_c^-$, within the accuracy of δ', the gap increment between consecutive equilibria. Except for the case $\Delta z = 0$, the vortices tilt with respect to the vertical direction. The vortices flatten in the x-direction, the direction along the axis joining the vortex centres, and elongate in the y-direction as the gap is decreased. Recall that the vortices have circular horizontal cross-sections as $\delta \to \infty$. Figure 4 shows the last equilibria found numerically for each Δz. We denote by δ^* the corresponding value of the gap δ. These states are strongly unstable.

We next investigate the nonlinear evolution of the unstable equilibria. We use contour surgery with the standard set-up of the method (Dritschel 1988; Dritschel & Saravanan 1994). The method is purely Lagrangian and the fluid domain is explicitly unbounded, consistent with the equilibria. We start with the equilibria shown in figure 3 for $\delta = \delta_c^-$. The contours bounding the vortices in mutual equilibrium are re-discretised using fewer nodes to reduce the computational cost of the contour surgery simulations while maintaining high accuracy. This re-discretisation introduces a small disturbance on the equilibria, enough to trigger the instability. The simulations are run until $t = 100$. We determine diagnostically the locations of the vortex centres

$$\boldsymbol{x}_i = \frac{1}{\mathcal{V}_i} \iiint_{\mathcal{V}_i} \boldsymbol{x}\, \mathrm{d}^3\boldsymbol{x}, \tag{2.9}$$

and the semi-axis lengths, $a \le b \le c$, of the best-fitted ellipsoids as functions of time. The best-fitted ellipsoid to a vortex is the ellipsoid having the same centre and the same second-order geometric moments as the vortex,

$$I_{mn} = \iiint_{\mathcal{V}_i} (x^m - x_i^m)(x^n - x_i^n)\, \mathrm{d}^3\boldsymbol{x}, \tag{2.10}$$

where we denote $(x, y, z) = (x^1, x^2, x^3)$ to simplify notations. Results are presented in figure 5. The values of the translation velocity V/q_r of these specific equilibria are recalled in table 2. In all cases, the dipole starts by translating at a constant velocity $V > 0$, and

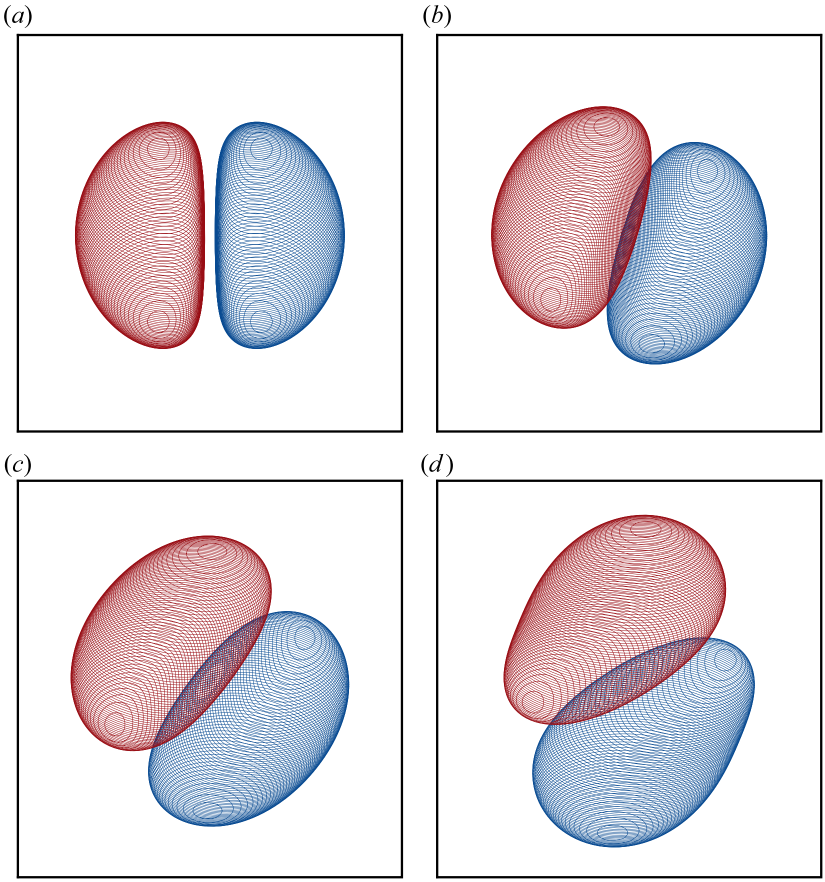

Figure 3. Vortex bounding contours for the relative equilibria at the margin of stability, for (*a*) $\Delta z/H = 0$, (*b*) $\Delta z/H = 21/83$, (*c*) $\Delta z/H = 41/83$, and (*d*) $\Delta z/H = 62/83$. The vortices are viewed orthographically at angle 60° from the vertical direction, in the $(x, y, zN/f)$ coordinate system.

the vortices deform little: the semi-axis lengths a, c, b remain constant initially. As the disturbances grow on the unstable equilibria, the vortices deform slightly as seen from the small variations of the semi-axis lengths in figures 5(*b*,*d*,*f*,*h*). This in turn affects their trajectories as seen in figures 5(*a*,*c*,*e*). For $\Delta z/H = 62/83$, vortex deformation occurs mostly in the limited region where the vortices occupy the same horizontal layers, and the weak deformation has a limited effect on the vortex centre trajectories. For $\Delta z/H = 21/83$, results are shown for $t \leq 85$ until a small debris detaches from vortex 2. The volume of the debris is only $1.6 \times 10^{-6}\mathcal{V}_2$. In all the other cases, the interaction is non-destructive. The vortices deform but retain their material, at least until the end of the simulation $t = 100$. It should also be noted that by $t = 100$, the dipoles have nearly travelled the distance $L = Vt$ that the undisturbed equilibria would have; see figures 5(*a*,*c*,*e*,*g*) and table 2. The instability hardly affects the dipoles overall, which is expected so close to the margin of stability.

We next turn our attention to the nonlinear evolution of the strongly unstable equilibria shown in figure 4, corresponding to $\delta = \delta^*$. In these cases, simulations are run until $t = 50$. A snapshot on the vortices at $t = 50$ is shown in figure 6. In all four cases, the interaction results in the destruction of the two vortices as they break into several secondary vortices

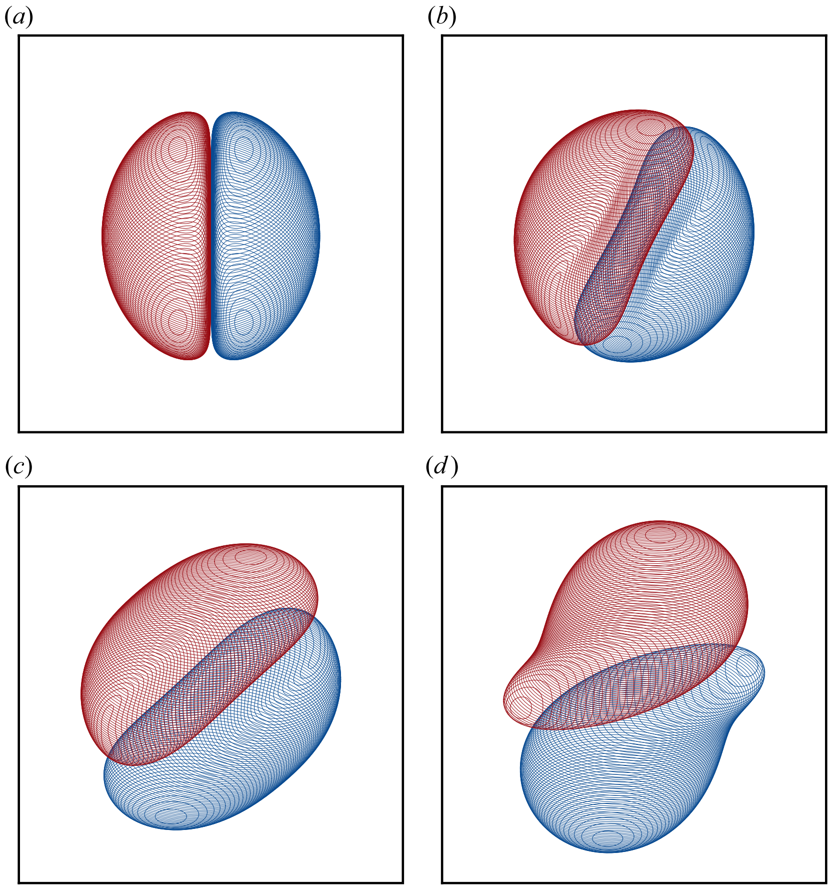

Figure 4. Vortex bounding contours for the last relative equilibria along the branch for $\delta = \delta^*$, for (a) $\Delta z/H = 0$, (b) $\Delta z/H = 21/83$, (c) $\Delta z/H = 41/83$, and (d) $\Delta z/H = 62/83$. The vortices are viewed orthographically at angle 60° from the vertical direction, in the $(x, y, zN/f)$ coordinate system.

$\Delta z/H$	0	21/83	41/83	62/83
V/q_r	0.0987	0.0868	0.0616	0.0278
$L(t = 100)$	62	54.5 (46.4)[a]	38.7	17.5

Table 2. Translation velocity V/q_r for the QG equilibria for $\delta = \delta_c^-$ shown in figure 3 and the distance $L = Vt$ that the undisturbed equilibria would travel until $t = 100$.

[a]At $t = 85$.

and a plethora of PV debris and filaments. For small vertical offsets, the interaction forms a mushroom-like structure, e.g. $\Delta z/H = 0$, 21/83. For large vertical offsets, $\Delta z/H = 41/83$, 62/83, part of the secondary vortices resemble hetons, or baroclinic dipoles. It should be noted that there is no dynamical asymmetry between cyclones $q > 0$ and anticyclones $q < 0$ within the QG model. In the cases considered here, the two vortices are initially symmetric. Contour surgery does not, however, enforce symmetry. While the numerical noise does not disturb the vortices symmetrically, some degree of symmetry

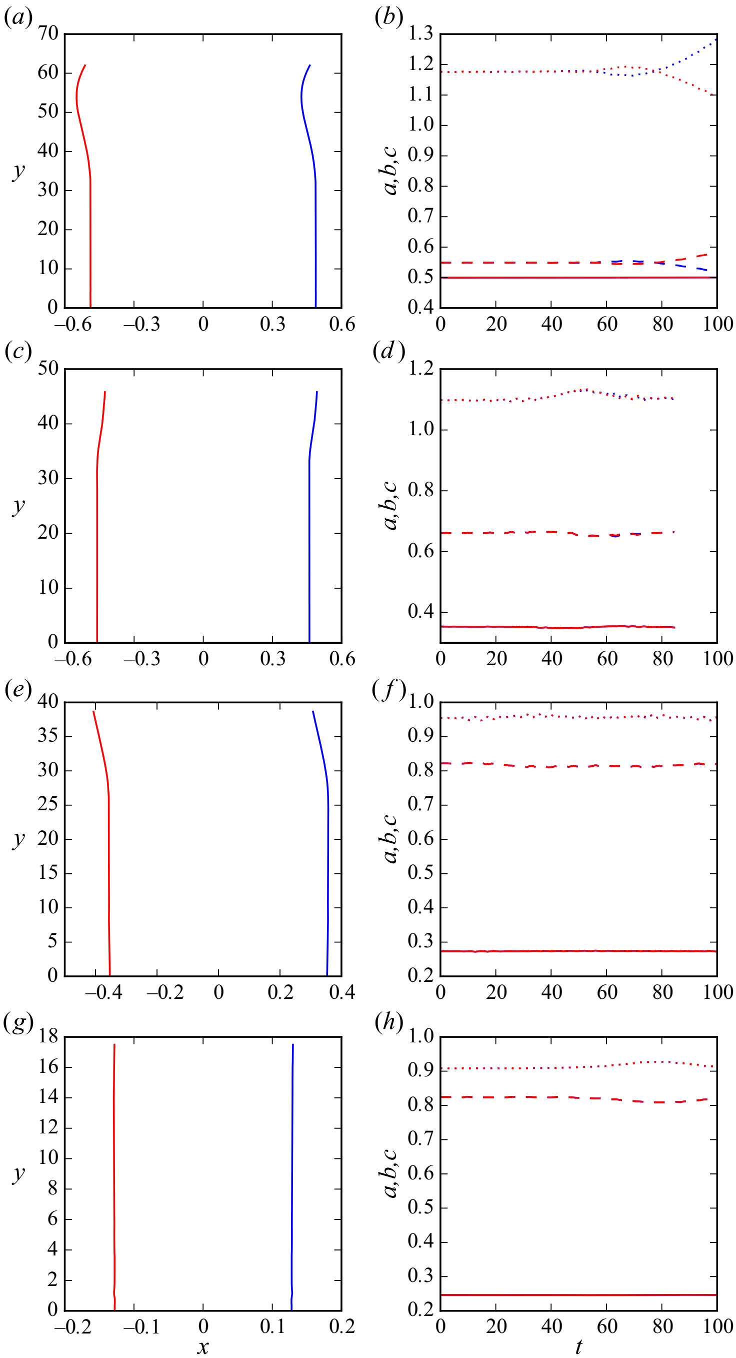

Figure 5. Vortex centre trajectories (*a*) and best-fitted ellipsoid semi-axes lengths (*b*) for the unstable QG equilibria for $\delta = \delta_c^-$ shown in figure 3(*a*) for $\Delta z = 0$. Similarly, (*c*,*d*) for $\Delta z/H = 21/83$, (*e*,*f*) for $\Delta z/H = 41/83$, and (*g*,*h*) for $\Delta z/H = 62/83$.

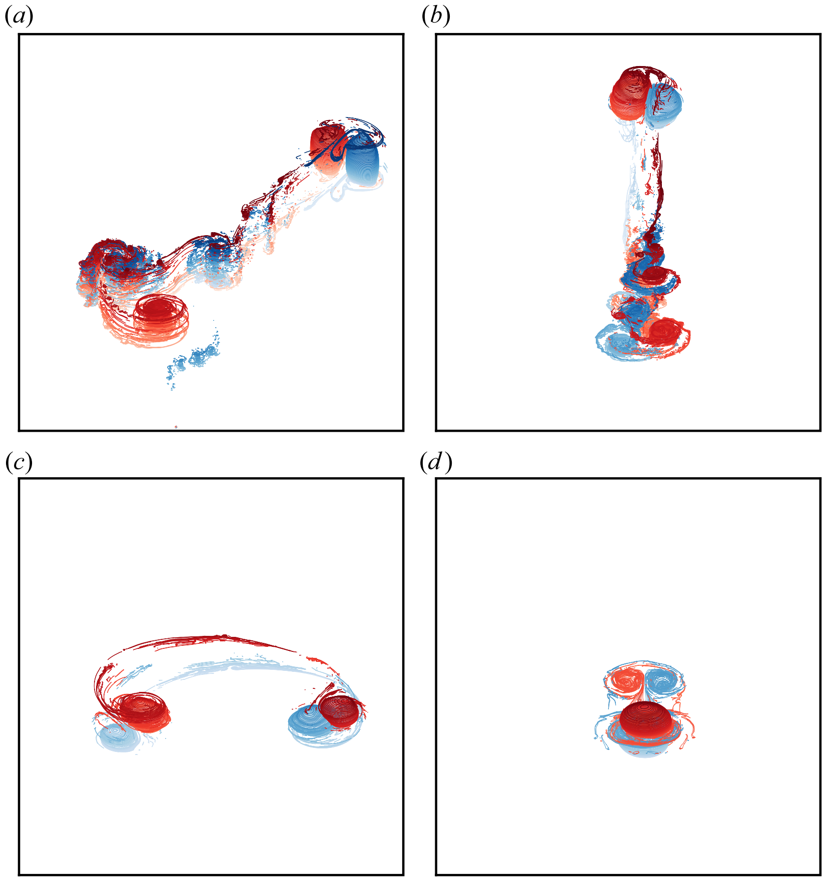

Figure 6. Vortex bounding contours for the nonlinear simulation of the unstable QG equilibria shown in figure 4 for $\delta = \delta^*$, for (a) $\Delta z/H = 0$, (b) $\Delta z/H = 21/83$, (c) $\Delta z/H = 41/83$, and (d) $\Delta z/H = 62/83$ at $t = 50$. The vortices are viewed orthographically at angle 60° from the vertical direction in the $(x, y, zN/f)$ coordinate system. The colour gradient indicates depth.

remains in the evolution of the vortices. The dynamical symmetry of the QG model breaks when adding the ageostrophic effects associated with a finite *Ro*. This is the focus of § 3.

3. Finite *Fr* and *Ro* vortices

We next consider the evolution of the pairs of vortices at finite *Fr* and *Ro*. Following Dritschel & Viúdez (2003), the prognostic equations are written in terms of Ertel's PV anomaly rescaled by N^2, q, which is conserved materially, and the horizontal part $\boldsymbol{A}_h$ of the vector quantity

$$\boldsymbol{A} \equiv \frac{\boldsymbol{\omega}}{f} + \frac{\nabla b}{f^2}, \tag{3.1}$$

where $\boldsymbol{\omega} = \nabla \times \boldsymbol{u}$ is the vorticity, b is the buoyancy anomaly, and $\boldsymbol{u} = (u, v, w)$ is the velocity.

The evolution equations for the variables q and $\boldsymbol{A}_h$ are

$$\frac{\mathrm{D}q}{\mathrm{D}t}=0, \tag{3.2}$$

$$\frac{\mathrm{D}\boldsymbol{A}_h}{\mathrm{D}t}+f\boldsymbol{k}\times\boldsymbol{A}_h=\frac{1}{f}(\boldsymbol{\omega}\boldsymbol{\cdot}\nabla)\boldsymbol{u}_h+\left(1-\frac{N^2}{f^2}\right)\nabla_h w-\frac{1}{f^2}\nabla_h\boldsymbol{u}\boldsymbol{\cdot}\nabla b, \tag{3.3}$$

where $\mathrm{D}/\mathrm{D}t\equiv\partial/\partial t+\boldsymbol{u}\boldsymbol{\cdot}\nabla$ is the material derivative, $\boldsymbol{k}$ is the vertical unit vector, and the subscript h denotes the horizontal part of a vector quantity. We next define a vector potential $\boldsymbol{\varphi}=(\varphi,\psi,\phi)$ associated with the vector $\boldsymbol{A}\equiv\Delta\boldsymbol{\varphi}$. Then we have readily

$$\boldsymbol{u}=-f\,\nabla\times\boldsymbol{\varphi}, \tag{3.4}$$

$$b=f^2\,\nabla\boldsymbol{\cdot}\boldsymbol{\varphi}. \tag{3.5}$$

The inversion relations to obtain $\boldsymbol{\varphi}$ are

$$\Delta\boldsymbol{\varphi}_h=\boldsymbol{A}_h, \tag{3.6}$$

$$\mathcal{L}_{QG}(\phi)-\left(1-\frac{f^2}{N^2}\right)\nabla\boldsymbol{\cdot}\frac{\partial\boldsymbol{\varphi}_h}{\partial z}+\frac{f^2}{N^2}\nabla(\nabla\boldsymbol{\cdot}\boldsymbol{\varphi})\boldsymbol{\cdot}\Big(\nabla^2\boldsymbol{\varphi}-\nabla(\nabla\boldsymbol{\cdot}\boldsymbol{\varphi})\Big)=q. \tag{3.7}$$

The fluid domain is a triply periodic box of dimension $[0,2\pi]^3$ in the $(x,y,zN/f)$ coordinate system. Following Dritschel & Viúdez (2003), PV is advected in a Lagrangian way. A fine 1024^3 grid is used to convert the Lagrangian PV field into a gridded Eulerian field. Equations (3.6) and (3.7) are then solved spectrally on a coarser Eulerian 256^3 grid. Nonlinear products are de-aliased using the 2/3 rule; see Orszag (1971). A small biharmonic diffusion is applied to the fields $\boldsymbol{A}_h$, such that the highest wavenumber is dumped at a rate $1+Ro_{PV}^4$ per initial period $T_{ip}=2\pi/f=T_{buoy}N/f=10$; see Dritschel & Viúdez (2003) and McKiver & Dritschel (2008). Further details of the method may also be found in Dritschel & Viúdez (2003).

The QG equilibrium vortices obtained in § 2 are used as initial conditions and are rescaled to fit the new layer thickness $\mathrm{d}z=2\pi/1024$. Simulations are spun-up using an initialisation phase where PV is smoothly ramped from $q=0$ to $q=f\,Ro_{PV}$ for the targeted PV-based Rossby number $Ro_{PV}=q/f$, minimising the generation of inertia-gravity waves; see Dritschel & Viúdez (2003) for details. In all cases, we set $f/N=0.1$. Dritschel & McKiver (2015) have shown that geostrophic turbulence depends only weakly on f/N at least for $f/N\lesssim 0.5$. Time is normalised by setting $N=2\pi$ so that the buoyancy period is $T_{buoy}=2\pi/N=1$. For each vertical offset Δz, we consider four values of the PV-based Rossby number $Ro_{PV}=0.1$, 0.3, 0.5 and 0.6. Simulations are run for the same QG-equivalent time, $T_{QG}=T(f/N)Ro_{PV}=50$. Equations are marched in time using the leapfrog scheme with time step $\Delta t=0.1$.

3.1. *Destructive interactions*

We first present examples of destructive interactions. For each Δz, the initial condition consists of vortices whose shape is given by the QG equilibrium for the smallest gap $\delta=\delta^*$ found in § 2 and shown in figure 4. Recall that these correspond to the ends of the branches of solutions obtained numerically. These are typically the most deformed vortices and are strongly unstable under the QG approximation.

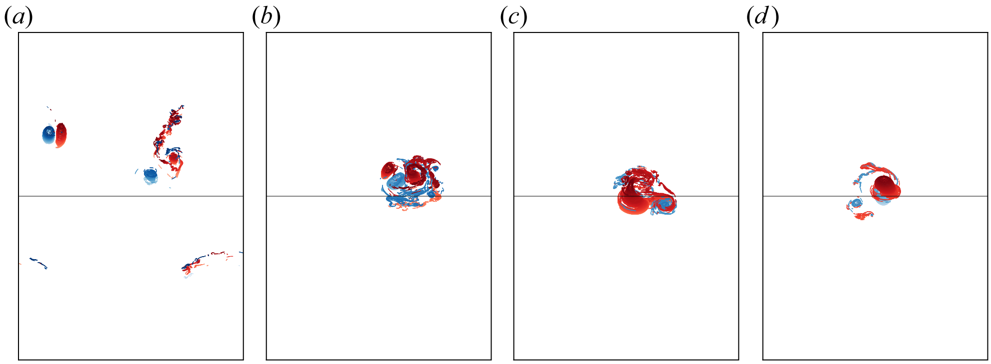

Figure 7. Vortex bounding contours shown orthographically at angle 45° from the vertical direction, for $(\Delta z/H, \delta) = (0, 21/83, 41/83, 62/83)$, and $Ro_{PV} = 0.5$ at $t_{QG} = 50$ for $\delta = \delta^*$.

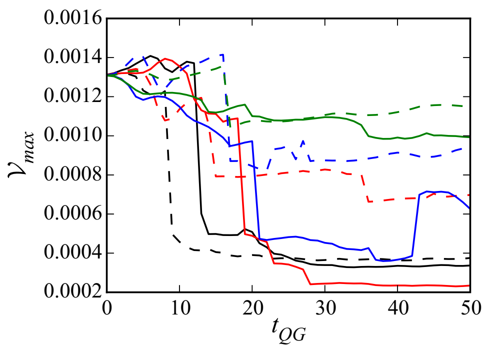

Figure 8. Evolution of the approximate volume of the largest cyclonic vortex (solid line) and anticyclonic vortex (dashed line) for $Ro_{PV} = 0.5$ and $\delta = \delta^*$, and $\Delta z/H = 0$ (black), 21/83 (red), 41/83 (blue) and 62/83 (green).

The shape of the vortices is given in figure 7 at $t_{QG} = 50$ for $Ro_{PV} = 0.5$. The interaction is, as expected, destructive. Indeed, in each case, the pair of vortices breaks into smaller secondary vortices and produces a large number of filaments and PV debris. This is generic of all destructive interactions, at all Ro_{PV}, when the initial conditions correspond to an unstable QG equilibrium. We measure the evolution of the approximate volume of the largest cyclone and the largest anticyclone in the flow. These are defined as the largest regions of contiguous positive and negative PV, respectively. The volume is evaluated using the vortex bounding contours redrawn on flat, equal-thickness layers, i.e. neglecting the deformation of the isopycnals. Results are shown in figure 8. They show that the largest anticyclone is larger than the largest cyclone by $t_{QG} = 50$ for all Δz. The anticyclone is expected to be more intense and to dominate the interaction, as argued below.

The evolution of the vortex pair for $\Delta z = 0$ is discussed further, and its evolution is presented, in figure 9. The cyclone first sheds a small amount of filaments at early times. Then the anticyclone sheds a medium-sized vortex in the wake of the dipole, while a part of the cyclone is entrained around the anticyclone, as shown in figure 9(*b*). Then the part of the cyclone surrounding the anticyclone is partially shed as a medium-sized vortex, formed to the right of the anticyclone, as seen in figure 9(*c*). A large filament is also shed

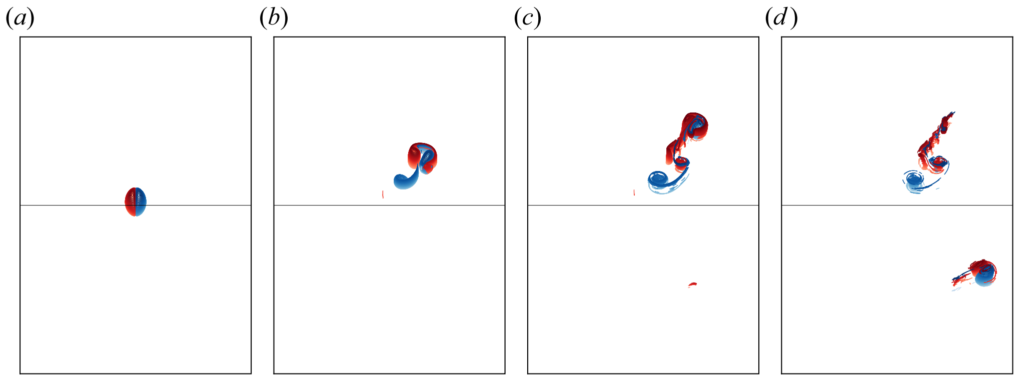

Figure 9. Vortex bounding contours shown orthographically at angle 45° from the vertical direction for $\Delta z = 0$, $Ro_{PV} = 0.5$, at $t_{QG} = 0, 10, 20, 30$ for $\delta = \delta^*$.

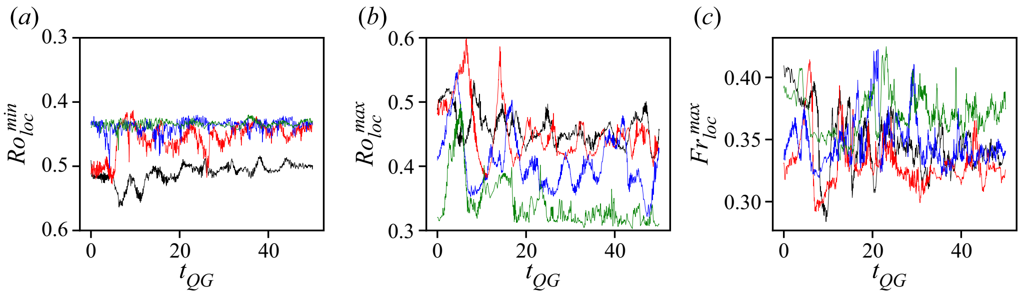

Figure 10. (*a*) Minimum and (*b*) maximum local Rossby numbers Ro_{loc}^{min}, Ro_{loc}^{min} and (*c*) maximum local Froude number Fr_{loc}^{max} versus time for $Ro_{PV} = 0.5$ for the cases shown in figure 9 for $\Delta z/H = 0$ (black), 21/83 (red), 41/83 (blue) and 62/83 (green).

$\Delta z/H$	$\overline{Ro_{loc}^{min}}$	$\overline{Ro_{loc}^{max}}$	$\overline{Fr_{loc}^{max}}$
0	−0.486	0.440	0.335
21/83	−0.438	0.434	0.314
41/83	−0.418	0.388	0.331
62/83	−0.415	0.326	0.354

Table 3. Time-averaged values for $Ro_{PV} = 0.5$.

by the pair of vortices. It is stretched in the wake of the dipole because its front end remains attached to the dipole, while its tails slows down as the dipole moves away.

We next consider the evolution of the extrema of vertical and horizontal vorticity. Figure 10 shows the evolution of the minimum and maximum local Rossby numbers $Ro_{loc}^{min} \equiv \min_{\mathcal{D}}(\zeta)/f$ and $Ro_{loc}^{max} \equiv \max_{\mathcal{D}}(\zeta)/f$, where ζ is the relative vertical vorticity, as well as the maximum local Froude number $Fr_{loc}^{max} \equiv \max_{\mathcal{D}}(|\boldsymbol{\omega}_h|)/N$, where $\boldsymbol{\omega}_h$ is the horizontal part of the relative vorticity $\boldsymbol{\omega}$. Results are shown for $Ro_{PV} = 0.5$ at $\delta = \delta^*$. The values fluctuate around means given in table 3. Results indicate that the time-averaged values of Ro_{loc}^{min}, Ro_{loc}^{max}, hence of the vertical relative vorticity ζ extrema, reach larger magnitudes in the anticyclone than in the cyclone.

The internal vertical potential ϕ for a unit sphere, in the $(x, y, Nz/f)$ coordinate system, of uniform PV q can be expanded in q following McKiver & Dritschel (2016), and reads

$$\phi = \frac{qr^2}{6} - \frac{q^2r^2}{27} + \frac{q^2r^2}{180}\left(\cos 2\theta - \frac{1}{3}\right) + o(q^2), \tag{3.8}$$

where $r = \sqrt{x^2 + y^2 + (zN/f)^2}$ is the radial coordinate and θ is the latitude. The external vertical potential reads

$$\phi = -\frac{q}{3r} + \frac{q^2}{54r^4} + \left(\frac{q^2}{30r^3} - \frac{q^2}{36r^4}\right)\left(\cos 2\theta - \frac{1}{3}\right) + o(q^2). \tag{3.9}$$

The horizontal components of the vector potential $\boldsymbol{\varphi}$ are zero in this case.

The first term in both equations corresponds to the QG solution. The leading correction term $-q^2r^2/27$ in (3.8) increases the magnitude of ϕ for an anticyclone ($q < 0$), while it decreases it for a cyclone ($q > 0$). Hence it is expected that the vertical relative vorticity ζ reaches higher values in the anticyclone.

Finally, the maximum Froude number Fr_{loc}^{max} is of the same order of magnitude as the maximum Rossby number, and we have the expected scaling $|\boldsymbol{\omega}_h|/N \sim \zeta/f$ and $\zeta/|\boldsymbol{\omega}_h| \sim f/N$, where $\zeta \sim U/L$, $|\boldsymbol{\omega}_h| \sim U/H$. Hence $H/L \sim f/N$.

To further analyse the evolution of the flow, we first define diagnostically two additional potentials, derived from the PV field q produced by the simulation at finite Ro, at any given time. We first define the QG potential $\boldsymbol{\varphi}_{QG} = (0, 0, \phi_{QG})$, obtained by inverting $\mathcal{L}_{QG}(\phi_{QG}) = q$. We also define a balanced potential $\boldsymbol{\varphi}_{bal}$, obtained using the nonlinear QG balance (NQG) derived by McKiver & Dritschel (2008). The balance relations in NQG include the ageostrophic corrections up to $O(Ro_{PV}^2)$. From these two potentials, we further define the imbalanced potential $\boldsymbol{\varphi}_{imb} = \boldsymbol{\varphi} - \boldsymbol{\varphi}_{bal}$ and the ageostrophic potential $\boldsymbol{\varphi}_{ageo} = \boldsymbol{\varphi} - \boldsymbol{\varphi}_{QG}$.

Figure 11 shows the imbalanced vertical velocity $w_{imb} \equiv -f\boldsymbol{\nabla} \times \boldsymbol{\varphi}_{imb} \boldsymbol{\cdot} \boldsymbol{k}$ for $Ro_{PV} = 0.5$, $\delta = \delta^*$ and $\Delta z/H = 0, 62/83$. The field allows one to observe the inertia-gravity waves generated by the vortex pair. We recover in the vertical cross-sections the typical St Andrew's cross pattern and the concentric horizontal wave patterns. Due to the periodic boundary conditions, we also see the waves generated by the period vortex images entering the computational box. It should be noted that to allow one to visualise the wave patterns, the figure limits the range of value of vertical velocity shown. As expected, the imbalanced vertical velocities are minimum/maximum in the vortices.

Figure 12 shows a vertical cross-section of the full rescaled, isopycnal displacement $\tilde{\mathcal{D}} = \mathcal{D}N^2/f^2$ across the vortex pair. Here, $\mathcal{D} \equiv -b/N^2$. For the anticyclonic vortex (right), $\tilde{\mathcal{D}} > 0$ for the vortex upper half, and $\tilde{\mathcal{D}} < 0$ for its lower half. The reverse is true for the cyclonic vortex on the left. Hence the anticyclone contains more mass even before the vortices start to break. It should be noted that the buoyancy anomaly associated with a QG spherical cyclone or anticyclone already shows the same trend for the associated buoyancy anomaly that it induces.

We next define the energy norm

$$\mathcal{E}_{tot} = \frac{\sqrt{\langle |\boldsymbol{u}|^2 + N^2\mathcal{D}^2\rangle}}{f} = \sqrt{\langle |\boldsymbol{\nabla} \times \boldsymbol{\varphi}|^2 + (\boldsymbol{\nabla} \boldsymbol{\cdot} \boldsymbol{\varphi})^2\rangle}, \tag{3.10}$$

where $\langle\cdot\rangle$ stands for the grid average. The same definition may be applied to all five fields $\boldsymbol{\varphi}$, $\boldsymbol{\varphi}_{bal}$, $\boldsymbol{\varphi}_{QG}$, $\boldsymbol{\varphi}_{imb}$, $\boldsymbol{\varphi}_{agoe}$ to define $\mathcal{E}_{tot}$, $\mathcal{E}_{bal}$, $\mathcal{E}_{QG}$, $\mathcal{E}_{imb}$, $\mathcal{E}_{ageo}$, respectively. The evolution

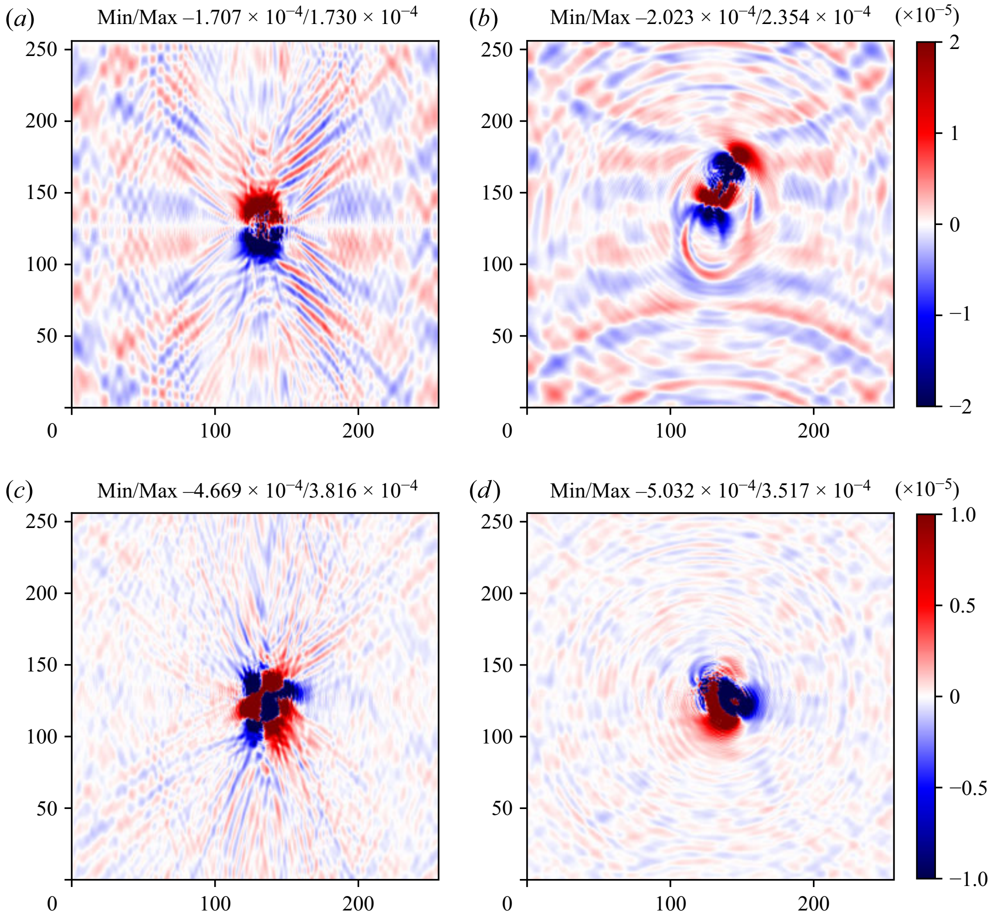

Figure 11. Imbalanced vertical velocity w_{imb} for $Ro_{PV} = 0.5$, $\delta = \delta^*$ and: (*a*,*b*) $\Delta z = 0$, $t_{QG=3}$, in (*a*) the (x, z)-plane at $y = 3.68$, (*b*) the (x, y)-plane at $z = 3.14$; (*c*,*d*) $\Delta z/H = 62/83$, $t_{QG} = 5$ in (*c*) the (x, z)-plane at $y = 3.14$, (*d*) the (x, y)-plane at $z = 3.14$. The actual min/max values are provided above the plots, and the ranges of values shown are indicated by the colour bars.

of the energy norms is shown in figure 13 for $\Delta z = 0$, $\delta = \delta^*$ and $Ro_{PV} = 0.1, 0.3, 0.5$ and 0.6. On the one hand, the curves $\mathcal{E}_{tot}$ and $\mathcal{E}_{bal}$ of the energy norm based on the full fields and the balanced energy norm are nearly indistinguishable, for all four values of Ro_{PV}. On the other hand, the imbalanced energy $\mathcal{E}_{imb}$ is nearly zero at all times. This means that the vortices remain in a near balanced state for all times. Recall that due to quadratic nature of the energy, $\mathcal{E}_{tot} \neq \mathcal{E}_{bal} + \mathcal{E}_{imb}$, even if, by construction, $\boldsymbol{\varphi} = \boldsymbol{\varphi}_{bal} + \boldsymbol{\varphi}_{imb}$. We also see, as expected, that as Ro_{PV} increases, a smaller part of $\mathcal{E}_{tot}$ is contained in the QG fields alone ($\mathcal{E}_{QG}$). The ageostrophic energy norm $\mathcal{E}_{ageo}$ also increases with Ro_{PV}.

Similar observations are made for $\Delta z \neq 0$ as shown in figure 14. Again, the full energy norm $\mathcal{E}_{tot}$ is almost identical to the balanced energy norm $\mathcal{E}_{bal}$, while the QG energy norm $\mathcal{E}_{QG}$ is roughly 90 % of $\mathcal{E}_{tot}$. While the flow has a non-negligible ageostrophic component, it remains balanced. We next turn out attention to non-destructive interactions.

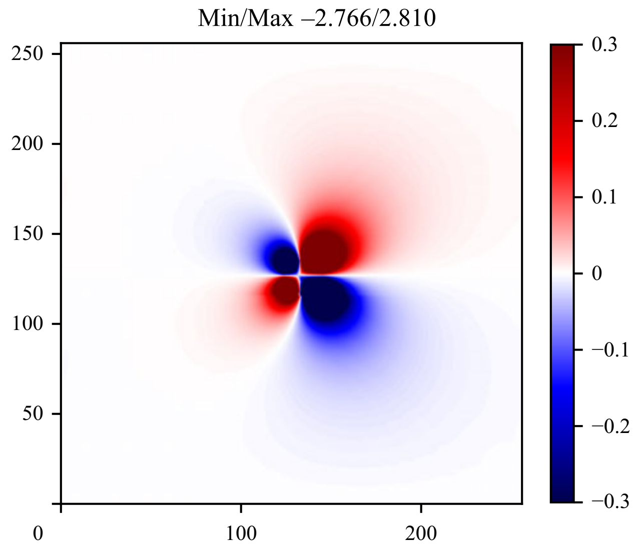

Figure 12. Rescaled isopycnal displacement $\tilde{\mathcal{D}}$ in the (x, z)-plane at $y = 3.68$ for $Ro_{PV} = 0.5$, $\delta = \delta^*$ at $t_{QG} = 3$.

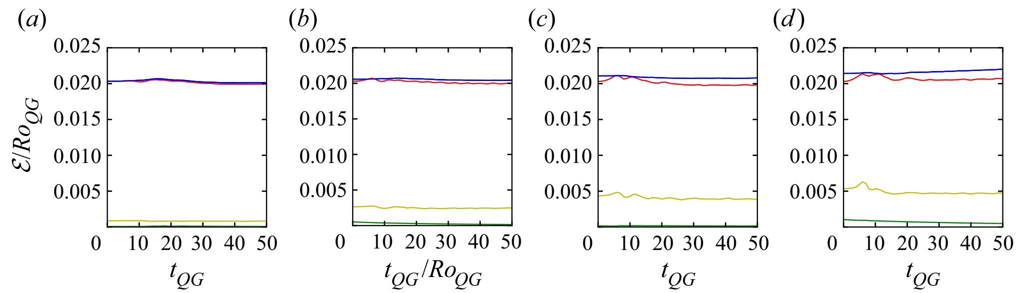

Figure 13. Evolution of the total 'energy norm' based on full fields ($\mathcal{E}_{tot}$, black), balanced fields ($\mathcal{E}_{bal}$, blue), QG fields ($\mathcal{E}_{QG}$, red), imbalanced fields ($\mathcal{E}_{imb}$, green) and ageostrophic fields ($\mathcal{E}_{ageo}$, yellow), for $\Delta z = 0$, $\delta = \delta^*$, and Ro_{PV} values (*a*) 0.1, (*b*) 0.3, (*c*) 0.5 and (*d*) 0.6. The blue and black lines are nearly identical.

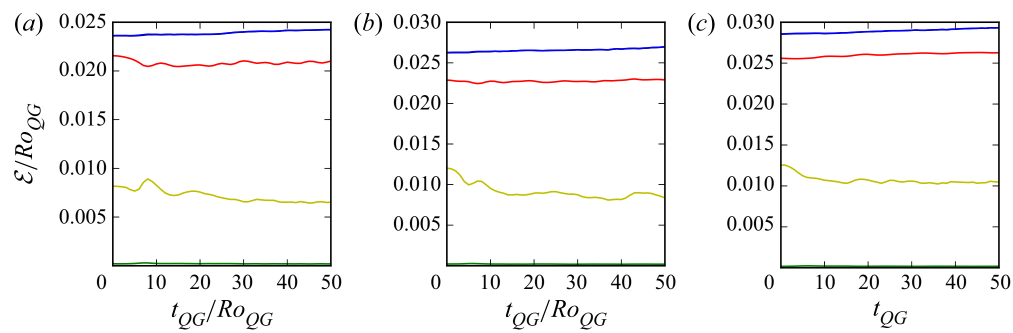

Figure 14. Evolution of the total 'energy norm' based on full fields ($\mathcal{E}_{tot}$, black), balanced fields ($\mathcal{E}_{bal}$, blue), QG fields ($\mathcal{E}_{QG}$, red), imbalanced fields ($\mathcal{E}_{imb}$, green) and ageostrophic fields ($\mathcal{E}_{ageo}$, yellow), for $Ro_{PV} = 0.5$, $\delta = \delta^*$ and $\Delta z/H$ values (*a*) 21/83, (*b*) 41/83, (*c*) 62/83. The blue and black lines are nearly identical.

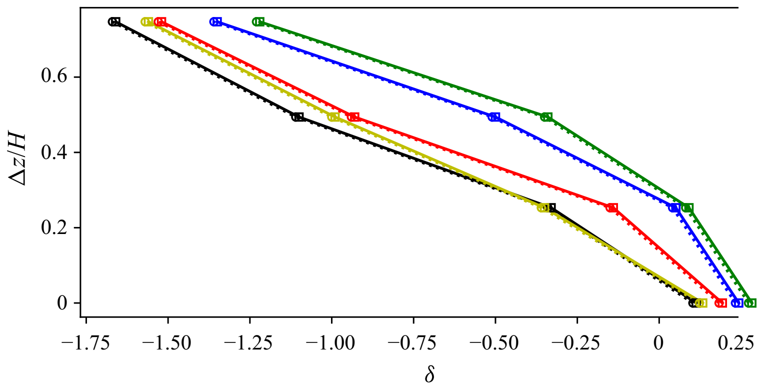

Figure 15. Values of bounds δ_n^+ (squares, solid line) and δ_n^- (circles, dotted line) for the limit of non-destructive interaction δ_n for $Ro_{PV} = 0.1$ (black), 0.3 (red), 0.5 (blue), 0.6 (green). Values of the bounds δ_c^+ (black squares) and δ_c^- (yellow circles) for the margin of linear stability for the QG equilibria are given for comparison.

3.2. *Elastic interactions*

We now focus on the ageostrophic effects when the interaction between the cyclonic and anticyclonic vortices is not destructive, but the vortices still deform. We first determine the smallest gap $\delta = \delta_n$ for which the two vortices retain their full volume, i.e. do not lose any material via filamentation, in the time window $t_{QG} \in [0, 50]$. Using the same convention as for the margin of stability of the QG equilibria, we denote δ_n^+ the smallest value of δ for our family of equilibria for which the interaction is non-destructive, and δ_n^- the largest value of δ for which filamentation occurs, i.e. $\delta_n^- < \delta_n < \delta_n^+$, with $\delta_n^+ - \delta_n^- = \delta' = 0.01$.

The values of δ_n^+ and δ_n^- are given in figure 15 for the four vertical offsets considered.

For $Ro_{PV} \geq 0.3$ and $\delta = \delta_n^-$, the vortices show relatively little deformation for $t_{QG} \in [0, 50]$, and are, in that sense, meta-stable. For example, figure 16 shows at $t_{QG} = 50$ the pair of vortices for $Ro_{PV} = 0.5$, $\delta = \delta_n^-$ and the four values of Δz. For $Ro = 0.1$, δ_n^- is close to the QG margin of stability, and by $t_{QG} = 50$, the vortices are strongly deformed, yet have not shed any material (result not shown). They would arguably undergo a destructive interaction at later time. Reaching much larger integration time is, however, impractical for low Ro_{PV} as it corresponds to a large effective time $t = t_{QG}N/(f\,Ro_{PV})$ while the time step is still controlled by the small buoyancy time scale.

The values of $\delta_n^\pm$ increase with Ro_{PV} for a given vertical gap Δz as the ageostrophic effects increase, making the vortices deform rapidly from the QG equilibria.

Similarly to the QG cases described in § 2, we determine diagnostically the centroid of each vortex. Figure 17 shows the vortex centre trajectories for $\delta = \delta_n^-$ for each values of Ro_{PV} and Δz considered. Recall that δ_n^- depends on both Ro_{PV} and Δz, therefore the value of δ_n^- is different in each panel of figure 17. A second series of vortex centre trajectories is presented in figure 18, where we use the same QG equilibrium for all Ro_{PV} for a given Δz. To ensure that all cases are non-destructive, but the vortices are close enough to interact as strongly as possible, we use for a given Δz the value $\delta = \delta_n^-(\Delta z, Ro_{PV} = 0.6)$, since $\delta_n^-(\Delta z, Ro_{PV} \leq 0.6) \geq \delta_n^-(\Delta z, Ro_{PV} = 0.6)$; see figure 15. Here, we see that increasing Ro_{PV} increases the curvature of the trajectory, indicating an increased dynamical asymmetry between the two vortices.

In all cases, the trajectory of the vortex centres is nearly circular. The trajectories are qualitatively similar to the trajectories of a pair of opposite-signed, unequal-strength QG

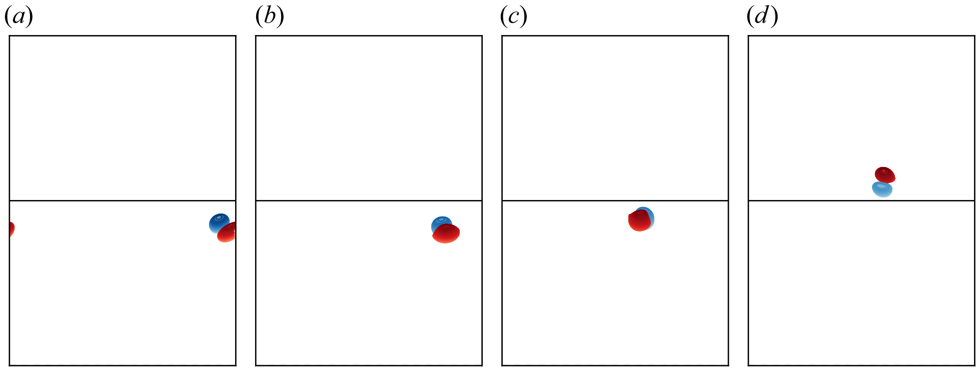

Figure 16. Vortex bounding contours viewed orthographically at angle 45° from the vertical direction, at $t_{QG} = 50$, $Ro_{PV} = 0.5$, $\delta = \delta_n^-$ and $\Delta z/H$ values (*a*) 0, (*b*) 21/83, (*c*) 41/83, and (*d*) 62/83.

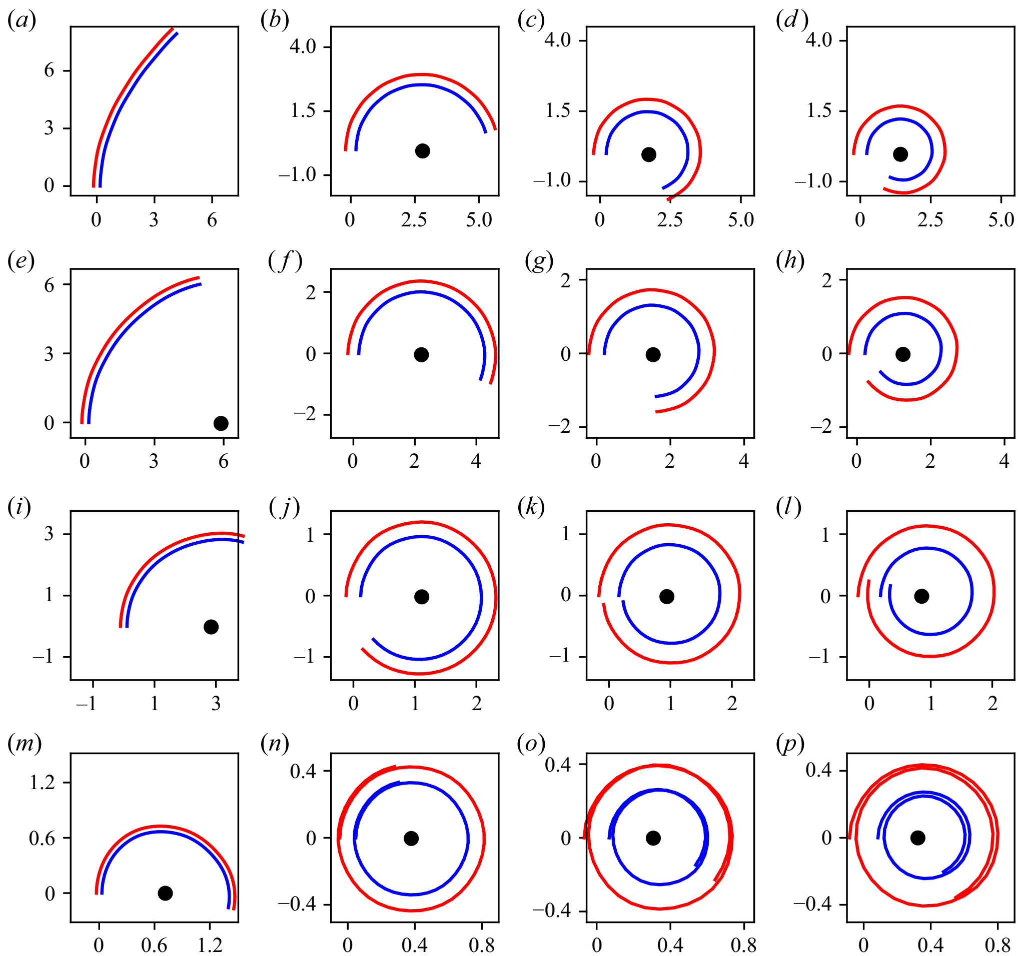

Figure 17. Trajectories of the vortex centres for $t \in [0, 50]$, $\delta = \delta_n^-$, $\Delta z = 0$ and Ro_{PV} values (*a*) 0.1, (*b*) 0.3, (*c*) 0.5, (*d*) 0.6; $\Delta z/H = 21/83$ and Ro_{PV} values (*e*) 0.1, (*f*) 0.3, (*g*) 0.5, (*h*) 0.6; $\Delta z/H = 41/83$ and Ro_{PV} values (*i*) 0.1, (*j*) 0.3, (*k*) 0.5, (*l*) 0.6; $\Delta z/H = 62/83$ and Ro_{PV} values (*m*) 0.1, (*n*) 0.3, (*o*) 0.5, (*p*) 0.6.

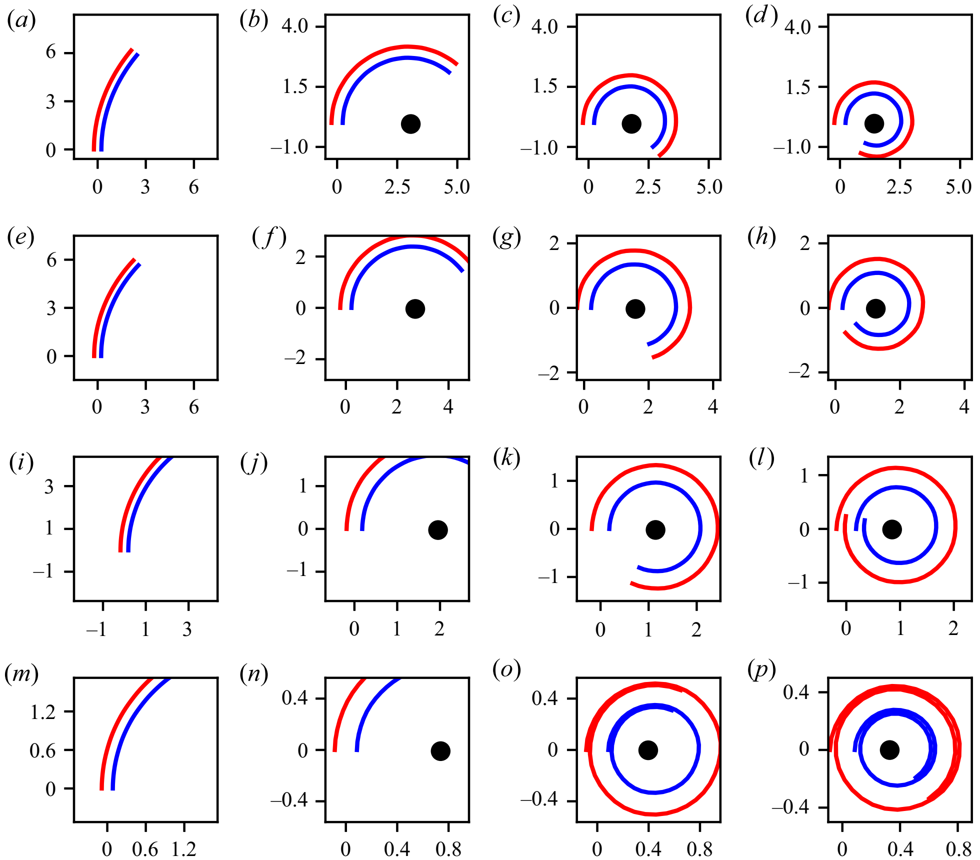

Figure 18. Trajectories of the vortex centres for $t \in [0, 50]$, $\delta = \delta_n^-(\Delta z, Ro_{PV} = 0.6)$, $\Delta z = 0$ and Ro_{PV} values (*a*) 0.1, (*b*) 0.3, (*c*) 0.5, (*d*) 0.6; $\Delta z/H = 21/83$ and Ro_{PV} values (*e*) 0.1, (*f*) 0.3, (*g*) 0.5, (*h*) 0.6; $\Delta z/H = 41/83$ and Ro_{PV} values (*i*) 0.1, (*j*) 0.3, (*k*) 0.5, (*l*) 0.6; $\Delta z/H = 62/83$ and Ro_{PV} values (*m*) 0.1, (*n*) 0.3, (*o*) 0.5, (*p*) 0.6.

point vortices. Recall that, however, the finite *Ro* and *Fr* vortices have equal Ertel's PV, in absolute value. They also stem from equal-volume QG vortices. The curvature of the trajectories is due only to the ageostrophic asymmetry between the cyclonic and the anticyclonic vortex. To have an indirect measure of this effect and be able to compare cases together, we define the QG-equivalent PV ratio ρ_{QG}^{equiv}, that is, the strength ratio of a pair of opposite-signed QG point vortices with the same circular trajectory. This is done as follows. For each non-destructive interaction that we have simulated numerically over the course of this study, we determine diagnostically the position of both vortex centres at 51 times, indexed from 0 to 50, every $\Delta t = 1$ for $0 \leq t \leq 50$. We select the position of the vortex centre, at three times, for each vortex, $\boldsymbol{x}_c^{i,j}$, where $i = 1, 2$ is the vortex index and j is the time index, $0 \leq j \leq 50$. This gives $2 \times 51 \times 50 \times 49$ triplets of vortex centre locations. For each location triplet, we determine the centre of the circle defined by the three points. The centre of the circle is the centre of rotation and coincides, by construction, with the strength centre for the equivalent QG point vortex pair. The latter can also be expressed as a function of the location of both vortices and their strength ratio, hence it allows one to determine the strength ratio from the locations. We then calculate the mean strength ratio,

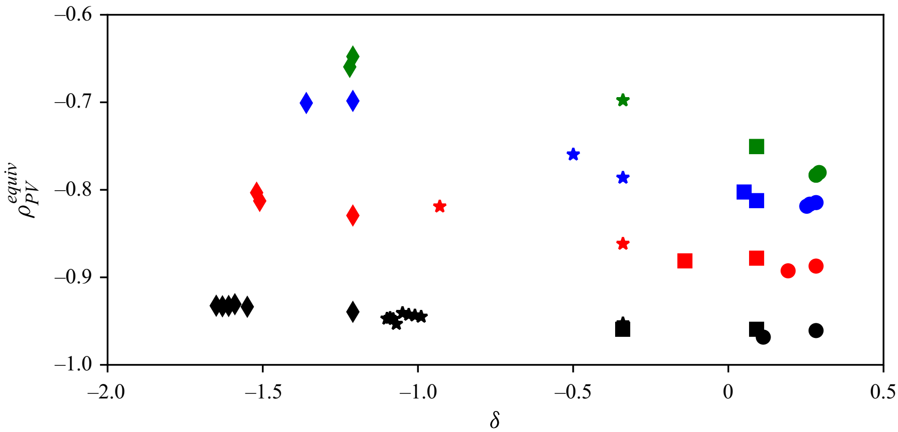

Figure 19. The QG-equivalent PV ratio ρ_{QG}^{equiv} versus the gap δ, for $Ro_{PV} = 0.1$ (black), 0.3 (red), 0.5 (blue), 0.6 (green), and $\Delta z/H = 0$ (circles), 21/83 (squares), 41/83 (stars) and 62/83 (diamonds).

averaging the values calculated over the full list of triplets, and all six possible pairs of x- and y-coordinates for the vortex centre within each triplets. Results are given in figure 19 for all non-destructive interactions. It should be noted that Pallàs-Sanz & Viúdez (2007) quantified the asymmetry between the two vortices by measuring the curvature of the trajectory.

The external streamfunction induced by a unit sphere given by (3.9), restricting attention, for simplicity, to the equatorial plane $\theta = 0$ of a vortex, is

$$\phi(r) = -\frac{q}{3r} + \frac{q^2}{45r^3} + o(q^2), \tag{3.11}$$

hence the azimuthal velocity induced by the single vortex is

$$u_\theta = -\frac{\partial \phi}{\partial r} = \frac{q}{3r^2}\left(1 - \frac{q}{5r^4}\right) + o(q^2). \tag{3.12}$$

By analogy with the QG solution, the factor $1 - q/5r^4$ can be interpreted as a ‘local’ PV correction to, hence for the dipole of PV, $q = \pm q_r$, $q_r > 0$, $\rho_{QG}^{equiv} \simeq -(1 - q_r/(5r^4))/(1 + q_r/(5r^4))$. This is a crude estimate as (i) the actual vortices of the pair are not spherical but deformed, and (ii) this estimate does not take into account the volume difference associated with the isopycnal displacement, which also favours the anticyclone. Figure 19 shows a relatively weak dependence of ρ_{QG}^{equiv} on δ, for a given Ro_{PV}, at least for the small range of δ considered. The same is true for the influence of Δz. One the other hand, ρ_{QG}^{equiv} depends strongly on $Ro_{PV} = q/f$. Increasingly, ρ_{QG}^{equiv} departs from -1 as Ro_{PV} increases, confirming the strengthening of the asymmetry with Ro_{PV}.

We finally estimate the evolution of the vortex deformation. To that purpose, and similarly to the analysis done in § 2, we measure the semi-axis lengths, $a \leq b \leq c$, of the vortex best-fitted ellipsoids. Again, the calculation is performed using the vortex bounding contours redrawn on flat, equal-thickness layers, i.e. neglecting the deformation of the isopycnals. Results are presented in figure 20. Since the equilibria stem from unit width-to-height aspect ratio vortices, and since the vortices elongate mostly along the y-direction, and flatten in the x-direction, the smallest semi-length, a, is in the x-direction,

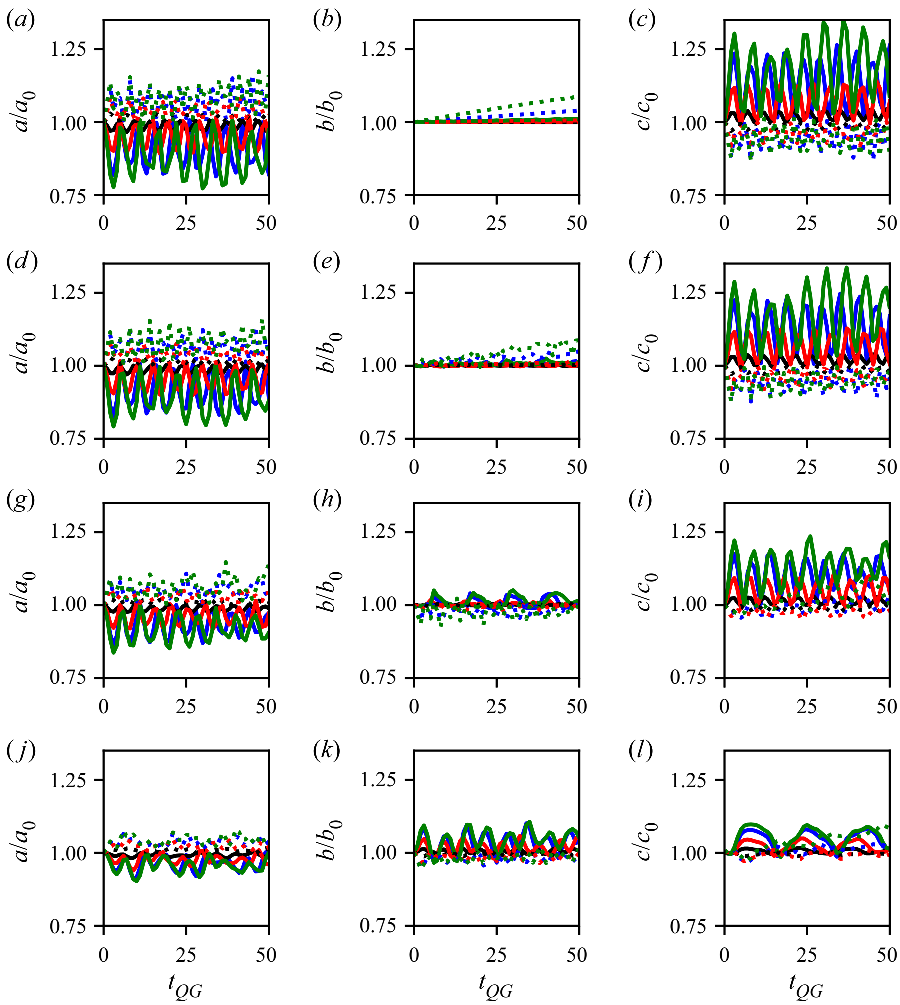

Figure 20. Evolution of best-fitted ellipsoids semi-axis lengths a/a_0, b/b_0, c/c_0 for $Ro_{PV} = 0.1$ (black), 0.3 (red), 0.5 (blue) and 0.6 (green). Solid (dashed) lines correspond to the cyclonic (resp. anticyclonic) vortex. For $\Delta z/H = 0$ and $\delta = \delta_n^-(Ro_{PV} = 0.6)$ (*a–c*), $\Delta z/H = 21/83$ and $\delta = \delta_n^-(Ro_{PV} = 0.6)$ (*d–f*), $\Delta z/H = 41/83$ and $\delta = \delta_n^-(Ro_{PV} = 0.6)$ (*g–i*). $\Delta z/H = 62/83$ and $\delta = \delta_n^-(Ro_{PV} = 0.6)$ (*j–l*).

and the largest semi-length, c, is in the y-direction. For small Δz, i.e. $\Delta z/H = 0, 21/83$, and $Ro_{PV} = 0.5, 0.6$, we see that b increases with time for the anticyclone. Since b initially corresponds to the semi-length along z, and the calculation ignores the displacement of the isopycnals, b can increase only if the vortex vertical axis tilts. Hence we observe a vertical tilt of the anticyclone for large Ro_{PV} and small Δz. Interestingly, a similar tilt was observed by Reinaud & Dritschel (2018) for pair of interacting co-rotating vortices. Overall, the oscillations observed for the 'horizontal' semi-lengths a and c indicate the pulsation of the vortices around a nearby quasi-equilibrium. The amplitude of the oscillations is larger for the cyclone, which is confirmed in figure 21, which shows the standard deviation of the normalised semi-axis lengths a/a_0, b/b_0 and $c/c0$. For larger Δz, the semi-length b also oscillates, indicating an oscillation of the vertical tilting of vortices. This is due to the increase in vertical shear as Δz increases.

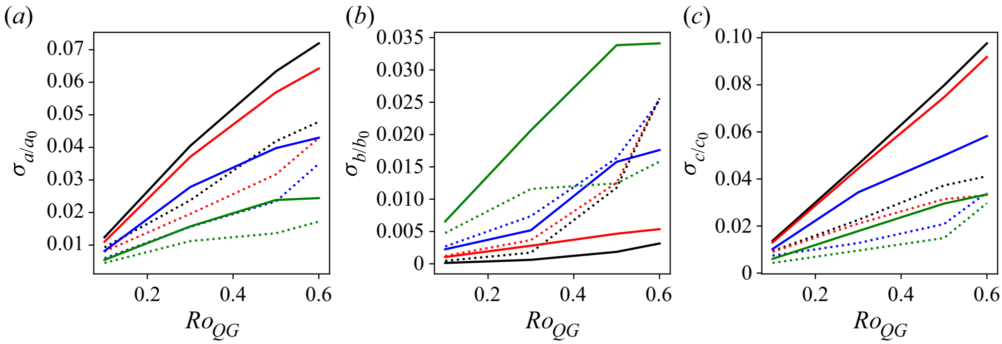

Figure 21. Standard deviation of the evolution of the best-fitted ellipsoids semi-axis lengths a/a_0, b/b_0, c/c_0 versus Ro_{PV} for $\Delta z/H = 0$ (black), 21/83 (red), 41/83 (blue), and 62/83 (green). Solid (resp. dashed) lines correspond to the cyclonic (resp. anticyclonic) vortex.

4. Conclusions

We have investigated the evolution of pairs of counter-rotating vortices at finite *Ro* and *Fr*. The initial conditions stem from a pair of equal-sized, unit width-to-height aspect ratio, equal and opposite uniform PV QG vortices in mutual equilibrium. The QG vortex pair may be linearly unstable if the vortices are close together. The instability leads to the deformation of the vortices, and the vortices may break into pieces. At finite *Ro* and *Fr*, the interaction can also lead to the destruction of the vortices if they are close enough together. In this case, the largest remaining vortex is typically an anticyclone. Remarkably, even during destructive interactions, the vortices remain close to a balanced state and emit only very few inertia-gravity waves. The flow may, however, contain a non-negligible ageostrophic part. At leading order, the ageostrophic effects tend to make an anticyclonic vortex more intense than a cyclonic vortex for the same PV, in absolute value. The isopycnals displacement also makes the anticyclone stronger than the cyclone.

The paper restricted attention to uniform PV vortices. The study could be extended to pairs of counter-rotating vortices with distributed, smooth internal PV distributions. Analysing how the smoothness of the PV field affects (i) the spontaneous generation of inertia-gravity waves and (ii) the stability/robustness of finite *Ro* and *Fr* vortices is of particular interest. Indeed, these have a direct impact on the dipoles' longevity, hence their ability to transport heat, salinity, moment and mass in the ocean. Another class of dipoles of interest is the hetons. An unpublished cursory study indicates that the heton may be sensitive to a baroclinic instability that may affect either the cyclonic vortex or the anticyclonic vortex more, depending on Ro_{PV}.

Finally, our choice of parameters and initial conditions leads to $Fr \sim Ro$. Exploring the full (*Ro*, *Fr*) parameter space is also of interest. For example, Billant, Dritschel & Chomaz (2006) were able to find common features for the instabilities affecting a Moore–Saffman elliptical vortex for small Froude number and arbitrary Rossby numbers. Whether such general features exist for pairs of opposite-signed vortices remains to investigated.

Declaration of interests. The author reports no conflict of interest.

Author ORCIDs.
Jean N. Reinaud https://orcid.org/0000-0001-5449-6628.

References

BILLANT, P., DRITSCHEL, D.G. & CHOMAZ, J.-M. 2006 Bending and twisting instabilities of columnar elliptical vortices in a rotating strongly stratified fluid. *J. Fluid Mech.* **561**, 73–102.

DRITSCHEL, D.G. 1988 Contour surgery: a topological reconnection scheme for extended integrations using contour dynamics. *J. Comput. Phys.* **77**, 240–266.

DRITSCHEL, D.G. & MCKIVER, W.J. 2015 Effect of Prandtl's ratio on balance in geophysical turbulence. *J. Fluid Mech.* **777**, 569–590.

DRITSCHEL, D.G. & SARAVANAN, R. 1994 Three-dimensional quasi-geostrophic contour dynamics, with an application to stratospheric vortex dynamics. *Q. J. R. Meteorol. Soc.* **120**, 1267–1297.

DRITSCHEL, D.G. & VIÚDEZ, À. 2003 A balanced approach to modelling rotating stably stratified geophysical flows. *J. Fluid Mech.* **488**, 123–150.

FEDOROV, K.N. & GINSBURG, A.I. 1989 Mushroom-like currents (vortex dipoles): one of the most widespread forms of non-stationary coherent motions in the ocean. In *Mesoscale/Synoptic Coherent Structures in Geophysical Turbulence. Proceedings of the 20th International Liège Colloquium on Ocean Hydrodynamics* (ed. J.C.J. Nihoul & B.M. Jamart), Elsevier Oceanography Series, vol. 50, pp. 1–14. Elsevier.

HOGG, N.G. & STOMMEL, H.M. 1985 The heton, an elementary interaction between discrete baroclinic geostrophic vortices, and its implications concerning eddy heat-flow. *Proc. R. Soc. Lond.* A **397**, 1–20.

KIZNER, Z., REZNIK, G., FRIDMAN, B., KHVOLES, R. & MCWILLIAMS, J. 2008 Shallow-water modons on the f-plane. *J. Fluid Mech.* **603**, 305–329.

LARICHEV, V.D. & REZNIK, G. 1976 Two-dimensional Rossby soliton: an exact solution. *Dokl. U.S.S.R Acad. Sci.* **231** (5), 1077–1080.

L'HEGARET, P., CARTON, X., AMBAR, I., MENESGUEN, C., HUA, B.L., CHÉRUBIN, L., AGUIAR, A., LE CANN, B., DANIAULT, N. & SERRA, N. 2014 Evidence of Mediterranean water dipole collision in the Gulf of Cadiz. *J. Geophys. Res.* **119** (8), 5337–5359.

MCKIVER, W.J. & DRITSCHEL, D.G. 2008 Balance in non-hydrostatic rotating stratified turbulence. *J. Fluid Mech.* **596**, 201–219.

MCKIVER, W.J. & DRITSCHEL, D.G. 2016 Balanced solutions for an ellipsoidal vortex in a rotating stratified flow. *J. Fluid Mech.* **802**, 333–358.

NI, Q., ZHAI, X., WANG, G. & HUGHES, C.W. 2020 Widespread mesoscale dipoles in the global ocean. *J. Geophys. Res.: Oceans* **125**, e2020JC01647.

ORSZAG, S.A. 1971 On the elimination of aliasing in finite-difference schemes by filtering high-wavenumber components. *J. Atmos. Sci.* **28**, 1074–1074.

PALLÀS-SANZ, E. & VIÚDEZ, À. 2007 Three-dimensional ageostrophic motion in mesoscale vortex dipoles. *J. Phys. Oceanogr.* **37**, 84–105.

REINAUD, J.N. 2019 Three-dimensional quasi-geostrophic vortex equilibria with m-fold symmetry. *J. Fluid Mech.* **863**, 32–59.

REINAUD, J.N. & DRITSCHEL, D.G. 2002 The merger of vertically offset quasi-geostrophic vortices. *J. Fluid Mech.* **469**, 287–315.

REINAUD, J.N. & DRITSCHEL, D.G. 2005 The critical merger distance between two co-rotating quasi-geostrophic vortices. *J. Fluid Mech.* **522**, 357–381.

REINAUD, J.N. & DRITSCHEL, D.G. 2009 Destructive interactions between two counter-rotating quasi-geostrophic vortices. *J. Fluid Mech.* **639**, 195–211.

REINAUD, J.N. & DRITSCHEL, D.G. 2018 The merger of geophysical vortices at finite Rossby and Froude number. *J. Fluid Mech.* **848**, 388–410.

REINAUD, J.N., DRITSCHEL, D.G. & KOUDELLA, C.R. 2003 The shape of vortices in quasi-geostrophic turbulence. *J. Fluid Mech.* **474**, 175–192.

DE RUIJTER, W.P.M., VAN AKEN, H.M., BEIER, E.J., LUTJEHARMS, J.R.E., MATANO, R.P. & SCHOUTEN, M.W. 2004 Eddies and dipoles around South Madagascar: formation, pathways and large-scale impact. *Deep-Sea Res.* (I) **51**, 383–400.

STERN, M.E. 1975 Minimal properties of planetary eddies. *J. Mar. Sci.* **33**, 1–13.

VALLIS, G.K. 2006 *Atmospheric and Oceanic Fluid Dynamics: Fundamentals and Large-Scale Circulation*. Cambridge University Press.

ZHANG, Z., WANG, W. & QIU, B. 2014 Oceanic mass transport by mesoscale eddies. *Science* **345**, 322–324.